Int. J. Electrochem. Sci., 11 **(2016)** 8459 – 8470, doi: 10.20964/2016.10.45

International Journal of
ELECTROCHEMICAL
SCIENCE
www.electrochemsci.org

Short Communication

Properties Research of Overlay Welding Treatment on Glass-lined Anticorrosion Tube with a Small Diameter

Guoqiang Xu

College of Pipeline and Civil Engineering, China University of Petroleum (East China), Qingdao 266580, P R China
E-mail: xuguoqiang@upc.edu.cn

Received: 24 May 2016 / *Accepted:* 27 July 2016 / *Published:* 6 September 2016

In this present study, the mechanical and anticorrosion properties of the Ni625 undercoat on 20# carbon steel prior to the welding process have been investigated by tensile, bending and hardness tests, and the electrochemical measurement. The absence of corrosion pits in the steels with Ni625 undercoat was investigated after CO_2 corrosion tests and the corrosion rate was assessed at $4.2x10^{-5}$ /mdd, revealing good anticorrosion qualities. Polarization surveys of the nickel materials in the chloride solutions displayed higher corrosion current densities relative to the situations of the steel, due to the high susceptibility to the pitting initiation on the nickel surface. Furthermore, Increasing the temperature of the corrosive environment from 30, 60 and 80°C displayed higher corrosion current densities and negative corrosion potentials, suggesting the enhanced corrosion events. Notably, the mechanical quality of Ni625 undercoat on carbon steel reached the requirements of the empirical applications, and this material revealed good selection for the overlay welding. In this regard, the selection of Ni625 undercoat for the weld overlay on carbon steel is good qualities in mechanical and anticorrosion properties.

Keywords: glass-lined tube; overlay welding; corrosion; mechanical properties

1. INTRODUCTION

Glass-line anticorrosion tube is widely used in the oil field due to effective corrosion protection properties against the corrosive electrolytes in the raw oils including chloride, sulfur and carbon dioxide [1-3]. In such corrosive electrolytes, the inner tube experiences the accelerated kinetics of corrosion events giving rise to localized pits. In addition, hydrogen generation by cathodic reactions during corrosion events leads to hydrogen brittleness of steel tube [4-5].

In terms of corrosion mechanisms of steel tube in the carbon dioxide environment, it is associated with the weak acid formation of H_2CO_3 in the following manners, $CO_2 + H_2O \rightarrow H_2CO_3$. Considering the presence of local defects of surface paints, H_2CO_3 can chemically attack the exposed steel substrate to generate the deposits of $FeCO_3$ and $CaCO_3$ and such deposits with the loose and porous structure cannot inhibit the proceeding corrosion at the localized defects. In addition, the galvanic corrosion can happen between defective and fine steel surface to encourage more corrosion events in the weak acidic electrolyte. Mao et al. [6] used the polarization survey and analytical electron microscopy to study corrosion behaviors of X-80 steel with dependence on the concentrations of HCO_3^- in the corrosive electrolytes. Interestingly, the pit absence was found when the HCO_3^- concentration was more than 0.05 M in the corrosive electrolyte and this phenomenon was in good agreement with the polarization survey. It suggested the increased anticorrosion property of X-80 steel in the HCO_3^- electrolyte when the concentration was more than 0.05 M. In contrast, the size and area of pits on the steel surface were increase when decreasing HCO_3^- concentrations as lower as 0.05 M, revealing an accelerated kinetics of corrosion events on the steel surface. For the situation, the HCO_3^- concentration-dependent corrosion kinetics on X-80 steel surface were associated with the availability of free hydrogen anions in the corrosive electrolyte and the higher concentration of HCO_3^- cations impeded the water hydrolysis giving rise to lower H^+ in the corrosive electrolyte.

In addition, chloride ions have revealed of significant influence on the polarization characteristics of tube steel due to the surface passive film disappearance by chloride attack. In terms of steel corrosion in the chloride solutions, the chloride concentration and ferrous oxides were the primary two limiting factors [7]. In the high-concentration chloride solutions (0.5-1 M), the corrosion rate of steel was decreased with the prolonged immersion in the corrosive electrolyte. This is attributed to the physical barriers of ferrous oxides, being the form of corrosion products, to inhibit mass transports including the ingress of the aqueous oxygen and inner ferrous anions. In contrast, the corrosion behaviors of steel when exposed in the 0.02-0.1 M Cl^- solutions displayed the distinct process of corrosion events. In the first three hours, corrosion rates were increased with the prolonged immersion time, which was dependent on the pit size. After this pitting initiation period, pits generally propagated on the whole surface giving rise to the decreased corrosion events in the similar behaviors of steel corrosion in the high concentration Cl^- solutions.

Considering the mixture of CO_2 and Cl^- environments, Xia et al. [8] used the deoxygenated mixture solution of CO_2-containing saturated NaCl brine to simulate the halide environment and employed electrochemical measurements to study the corrosion process of carbon steels. Initially, steel corrosion generated a surface of an intact film, being the form of corrosion product of $Fe(HCO_3)_2$. However, corrosion products experienced transmission to form the loose and porous products of $Fe(CO_3)_2$ after the prolonged steel immersion in the simulated halide environments. Thus, the corroded carbon steel in the mixture corrosive electrolytes were associated with the coupling effects of different parts of carbon steels, which may be influenced by the coverage of corrosion products. Furthermore, Palacios et al. [9] revealed corrosion events with dependence on steel microstructures during immersion in the mixture solution of CO_2-saturated NaCl brine. Importantly, steel microstructure determined the adhesiveness of corrosion products with substrate. In comparison with tempered and quenched steels, the corrosion scales on the normalized steel displayed better adherence and bigger

thickness on the corroded surface. For this situation of the normalized steel, the cavities between pearlite phases allowed the local Fe^{2+} enrichment and the local flow stagnation determined the formation of an iron carbonate scale.

In terms of glass-line tube process, the enamel glaze was used to generate a surface of inner glass covering carbon steel at high baking temperature and this intact film is of ~1.5 cm thickness [10, 11]. In this sense, glass-line tube provides good quality of mechanical property by the carbon steel, whilst maintaining effective anticorrosion by a surface of inner glass. However, the enamel glass can melt during welding treatment due to the localized high temperature giving rise to expose the substrate steel and to decrease the anticorrosion property at the jointing parts. Considering such potential threats by the welding treatment, the overlay welding of a surface of anticorrosion alloys was suggested to pre-treat the end of carbon steel before the sputtering spray of glass [12]. Han et al. [13] successfully used the welding wire of Ni625 for the overlay welding treatment of carbon steel to generate an inner film of 36 mm in width prior to the glass-line process and welding treatments. Electron probe microscope revealed three layers at the jointing part, including cellular-dendrite root layer, a transition layer of martensite and retained austenite, and the capping layer of acicular ferrite and pearlite. Furthermore, the more Ni concentration at the root layer than that in the inner jointing parts provided effective anticorrosion property of the overlay welding treatments. However, the information of the overlay alloys during the corrosion tests in the CO_2 environment and the associated corrosion rates are not unknown, which are of great significance in the empirical engineering. Thus, our present study used the weight-loss method to assess and compare the corrosion rate of the treated tube and joints with the untreated carbon steel. Furthermore, electron microscopy and mechanical properties tests were also used to investigate the microstructure and metallurgical properties of joint parts.

2. EXPERIMENTAL

2.1. Material and preparation

20# carbon steel, of 35x15x3 mm, was prepared by wire-electrode cutting, and Table 1 and 2 show the composition and mechanical properties of carbon steel respectively. In terms of substrate pre-treatment, it consists of mechanical polishing to 800 grit SiC finish, rinsing by ethanol and deionized (DI) water, and cool-air stream drying. Before corrosion tests, the sample weight was scaled as a reference and samples were sealed by silica gel. Table 3 displays the chemical composition of the welding wire of AT·ERNi625 (NiCrMo-3) with a diameter of 1.2 mm. The parameters of the overlay welding include the welding current of 145 A, welding rate of 130 mm/min, wire feeding rate of 1.0 m/min, overlapping ratio of 50%, the overlay width of 15 mm, and the overlay thickness of 1 mm.

Table 1. Nominal compositions (wt. %) of 20# carbon steel

C	Mn	Si	S	P	Cr	Ni
0.12	1.44	0.37	0.004	0.017	0.05	0.03
Cu	Mo	V	Ti	B	Nb	Fe
0.10	0.01	0.0045	0.028	0.0002	0.038	Balance

Table 2. Parameters of the mechanical properties of 20# carbon steel

Tensile Strength /MPa	Yield Strength /MPa	Elongation /%
253-500	275	25

Table 3. Nominal compositions (wt. %)of the welding wire, AT·ERNi625, by weight

C	Si	Mn	Cr	Fe	Ni	P
0.017	0.23	0.08	21.35	1.31	63.10	0.01
S	Mo	Nb	Ti	Al	Cu	Others
0.003	8.6	3.68	0.06	0.30	0.03	0.23

2.2. Characterizations

Corrosion behaviors of the overlay alloys in the CO_2 were investigated by magnetic-driven FCZ reactor at the accelerated environment of high temperature and high pressure. The prior ventilation of CO_2 was used for 1 h to create the deoxygenated environment before corrosion tests. The temperature of 60 °C and CO_2 pressure of 4 MPa, rotation rate of 1 m/s, test duration of 20 d were used at the test parameters. Composition of corrosive electrolyte has been shown in Table 4. The weight loss measurement of samples before and after corrosion tests was used to assess the anticorrosion properties [14].

Table 4. Chemical compositions of the corrosive electrolytes used in CO_2 corrosion reactors for the overlay alloys

Compositions	NaCl	$CaCl_2$	$MgCl·6H_2O$	$NaHCO_3$	DI water
Weight %	0.1596	0.0512	0.02	0.116	0.6532

In terms of polarization survey of the overlay alloys, a three-electrode system was used in PARSTAT2273 electrochemical workstation in FCZ10-22/250 reactor. A three-electrode cell was employed, with a saturated calomel electrode (SCE, E^o=0.24 V vs. NHE), a graphite electrode and a working electrode of the exposed area of ~1 cm^2. Before polarization survey, the corrosive electrolyte (composition as Table 4) was deoxygenated by CO_2 for 1 h, and the temperature influence of 30, 60 and 80 °C on the polarization behaviors of the overlay alloys was studied. The specimens were immersed in the corrosive electrolyte under open-circuit potential for 30 min to reach a steady OCP level. Subsequently, the potentiodynamic scan was employed from -0.25 to 0.25 V vs. OCP at the scanning rate of 0.5 mV/s.

Mechanical properties of 20# carbon steel with a surface of Ni625 overlay, of 230x76x6 mm, included tensile strength, three-point bending (face and root bending) and micro hardness. According

to GB/T 228.1-2010 <Tensile test methods for metallic materials>, tensile strengths of 20# carbon steel and steel with overlay alloys were measured in a Wdw300 electronic universal testing machine at the rate of 1 mm/min. The bending tests were used to detect the mechanical properties of the samples under bending loads, including face and root bending test, and the visible check of surface cracks after bending tests. According to GB/T 2653-2008 <Bending test methods for welded joints>, the steel with overlay alloys of Ni625 was under bending loads at the displacement rate of 1 mm/min.

JSM-6380LA scanning electron microscopy, with an accelerating voltage of 20 kV, was used to investigate the morphology of the joint fractures, ,which were prepared with overlay alloys on the top.

V-1000A hardness tester was used to detect the hardness in micro-size, and the detected samples were mechanically polished to 800 grit SiC finish and rinsed by ethanol and DI water, and cool-air stream drying. The hardness measurement started from the fusion line and then moved in the vertical direction relative to fusion line to the base material and weld overlay in a step of 0.2 mm until the constant hardness was revealed.

3. RESULTS AND DISCUSSION

3.1. Corrosion behaviors

Table 5 shows the results of weight loss tests of two samples ejecting in the CO_2 environment. After corrosion tests for 20 d, the average rate of sample corrosion was ~$4.3\pm0.1x10^5$ mdd. In contrast, the reported corrosion rate of carbon steel in the same CO_2 test was 1.2 mdd [15-17]. In this regard, the overlay alloys of Ni625 revealed the effective corrosion resistance in the CO_2 environments. Furthermore, the top view macrograph in Figure 1 displayed the absence of general corrosion on the sample surface after the 20 d-CO_2 corrosion test. Considering the metal reactivity, the standard potentials of Ni/Ni^{2+} and Fe/Fe^{2+} reactions were -0.25 and -0.44 V_{NHE} respectively [18] and, hence, the noble nickel overlay alloy can provide the effective anticorrosion properties in the corrosive CO_2 environment.

Table 5. Weight loss results of the overlay alloys after CO_2 corrosion test

Sample codes	Length /mm	Width /mm	Thickness /mm	Mass before corrosion /g	Mass after corrosion /g	Corrosion rate /mdd	Average corrosion rate /mdd
1	23.86	14.70	2.90	12.7536	12.7517	0.0000413	0.0000428
2	23.53	14.62	2.90	12.6691	12.6671	0.0000443	

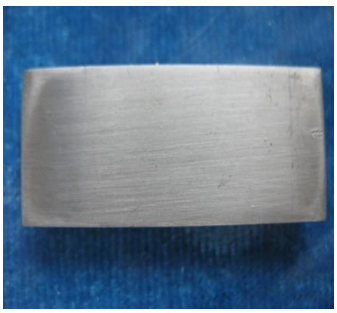

Figure 1. Optical image of the sample surface after corrosion test

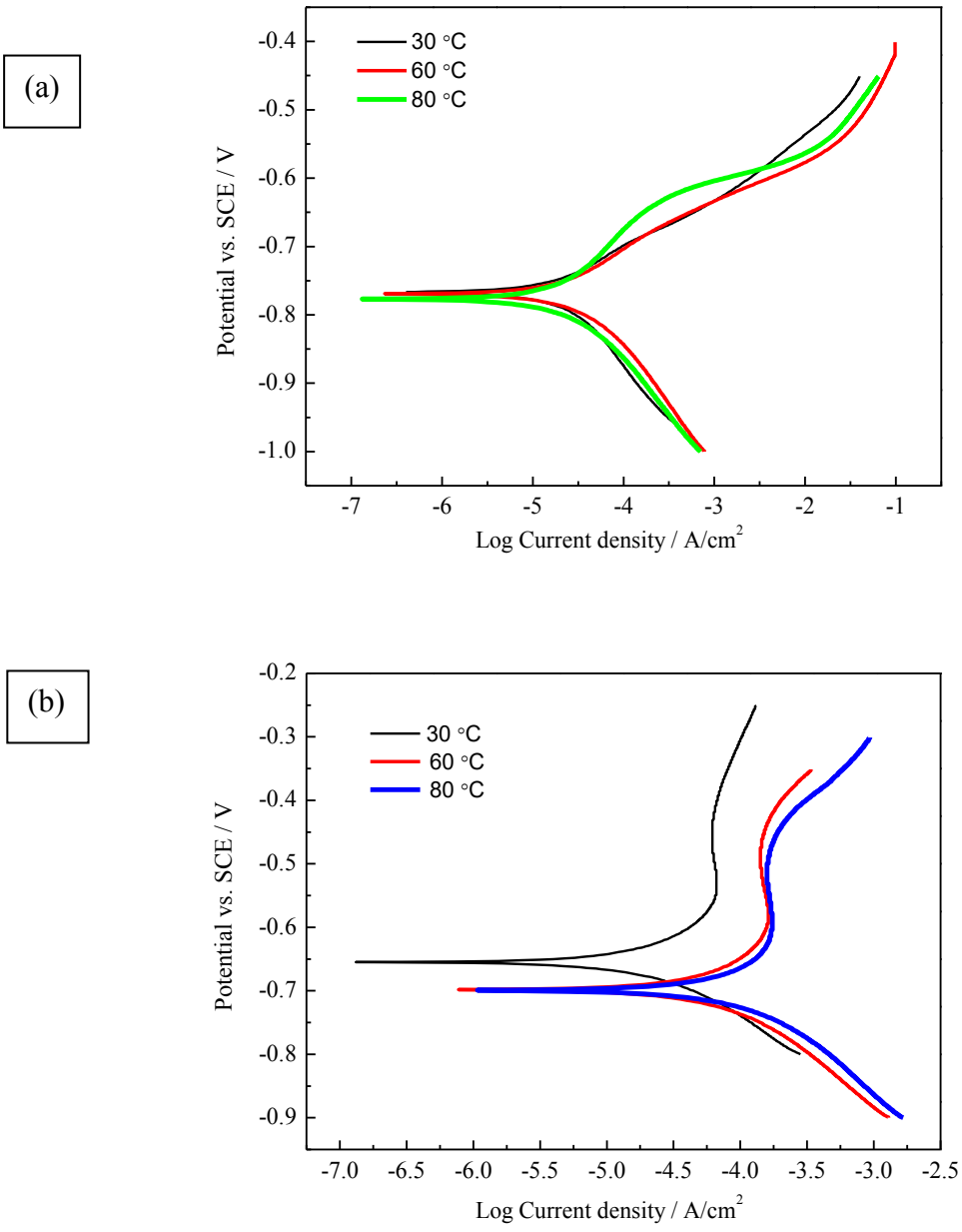

Figure 2. Polarization surveys of (a) 20# carbon steel and (b) the overlay alloy of Ni625 in the chloride solutions with dependence on the temperatures of 30, 60 and 80 °C as outlined by black, red and blue lines respectively.

Figure 2 shows the polarization surveys of 20# carbon steel and the overlay alloys of Ni625 and Table 9 displays the measured results of corrosion potential and current densities according to the plots.

Considering the cathodic reaction of oxygen reduction, the cathodic polarization surveys of both substrates revealed the evident positive shift with increasing temperature, especially for the overlay alloys of Ni625. For example, at -0.75 V_{SCE}, the increased order of cathodic current densities was as follows, $10^{-3.9}$ (30 °C) < $10^{-3.8}$ (60 °C) < $10^{-3.6}$ (80 °C). In Table 6, increasing solution temperature revealed a proportional increase of corrosion events as evidenced by the negative shifts of corrosion potentials and higher current densities. This tendency indicated the enhanced corrosion kinetics in the corrosive environment at a higher temperature [19]. Interestingly, the overlay alloys of Ni625 displayed higher corrosion current densities in the chloride solutions relative to the situations of carbon steel and it is associated with the chloride sensitivity difference between nickel and steel materials. In comparison with carbon steel, the nickel overlay is susceptible to the pitting and localized corrosion and this is widely reported in the literature [20-22].

Table 6. Corrosion potentials and current densities of 20# carbon steel and overlay alloys of Ni625 during polarization surveys in chloride solutions with dependence on temperatures.

Materials	Temperature / °C	Corrosion potential / V_{SCE}	Current densities / A/cm^2
20# carbon steel	30	-0.767	1.845x10-5
	60	-0.769	2.41x10-5
	80	-0.777	2.577x10-5
Overlay alloy of Ni625	30	-0.611	4.255x10-5
	60	-0.698	1.103x10-4
	80	-0.699	1.879 x10-4

3.2. Mechanical properties of the steel with weld overlay

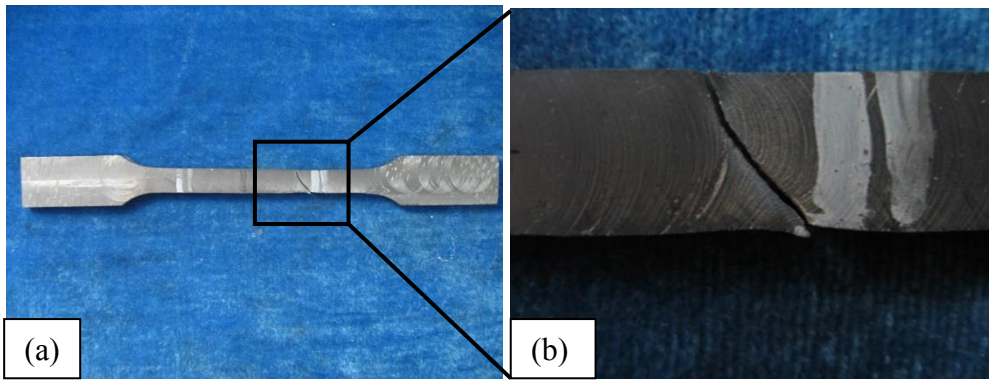

Figure 3. Optical images of the detected samples after tensile tests, (a) low- and (b) high-magnification images.

Figure 3 shows the optical macrographs of the detected samples after tensile tests, and the evident necking was observed near tensile fracture. Furthermore, the results of tensile tests have been shown in Table 7, including the single 20# carbon steel and the steel with the nickel overlay. Notably, the better mechanical properties of the steel with the weld overlay were observed in comparison with the situations of carbon steel. For example, the extensibility limits of two steels with the weld overlay of Ni625 were 30-40.6 %, while 27.2% for the single carbon steel. According to the requirements of GB/T 9711-2011 <Steels for petroleum and natural gas industrial pipeline transportation system>, the steels after overlay welding process are good for the applications.

Table 7. Results of tensile tests

Sample codes	Materials	Yield Strength /MPa	Tensile Strength /MPa	Elongation /%
1	Ni625 overlay	365	575	30.0
2	Ni625 overlay	365	600	40.6
3	20# carbon steel	270	460	27.2

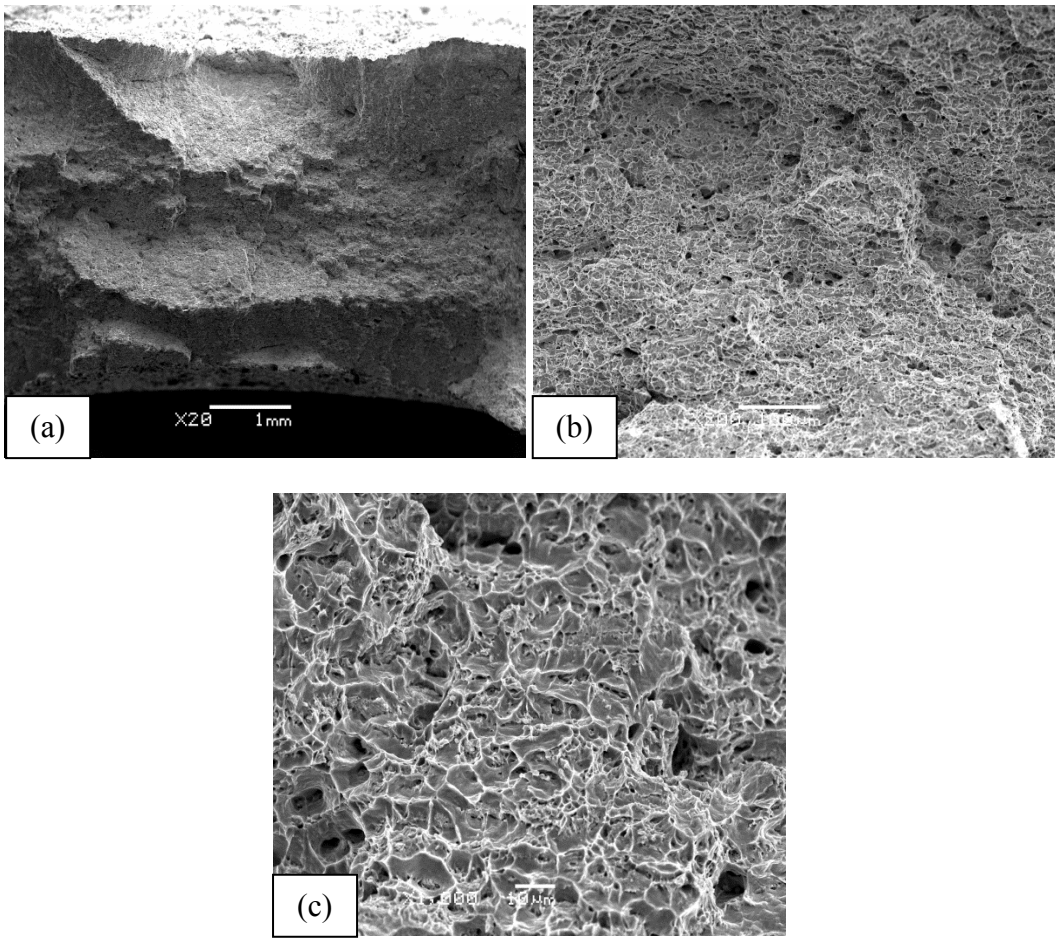

Figure 4. Scanning electron micrographs of tensile fracture of the weld overlay. (a), the low-magnification images of the tensile fracture; (b), microstructure image at 200x; (c), microstructure image at 1000x.

Scanning electron micrographs of tensile fracture are shown in Figures 4, including the low- and high-resolution images. In Figure 4a, the top was the base materials while the weld overlay was at the bottom. In contrast, the ductile fracture was observed at the base materials as evidenced by the fibrous characteristics. In terms of microstructure analyses in the high-resolution images (Fig. 4b and 4c), the honeycomb structure was investigated at the tensile fracture, including the popular dimples in the small sizes. For this situation, the dimple fracture was associated with the presence of precipitates, inclusions, sub grain boundaries, grain boundaries and the dislocation accumulation in the base materials, and increasing the tensile loads gave rise to the localized plastic deformations to generate the dimple fractures [23]. This morphology at the tensile fracture was due to the ductile fracture created by the plastic deformation, and this is in good agreement with the good quality of extensibility.

Figure 5. Optical images of the detected samples after bending tests

Figure 5 shows the optical macrographs of the detected samples after bending tests, and Table 8 displays the bending results of steels with the weld overlays. Notably, the absence of surface defects after both bending tests at bending angles of 180° revealed the good ductility. This is consistent with the earlier SEM results for good mechanical qualities of the steels with the weld overlays.

Table 8. Results of face and root bending of steels with the weld overlays

Sample codes	Tests	Thickness /mm	Bending diameter /mm	Bending angle /°	Defect length /mm
1	Face bending	4	30	180	0
2	Face bending	4	30	180	0
3	Root bending	4	30	180	0
4	Root bending	4	30	180	0

Figure 5 shows the evolution of micro hardness with dependence on the locations of the welding joints and the results are presented in Table 9. The maximum hardness was observed near the fusion line, associated with the heat affected zones. In contrast, the lower hardness was detected at the base materials far away from the fusion line. For the situation, it was associated with the heat affected zones during Tungsten argon arc welding process at the temperature of more than 1000 °C. In contrast, the temperature of Ac3 of 20# carbon steel is 830-850 °C and, hence, the welding process played a role of quenching treatment for the carbon steel. In comparison, the welding process leads to the burning damage of the Ni625 overlay and the worse was observed at the topper layer of the joint part. In this sense, the micro hardness at the base materials far away from the fusion line appeared the lower levels.

Table 9. Hardness results of steels with the weld overlays

Distance relative to fusion line /mm	-1.0	-0.8	-0.6	-0.4	-0.2	0	0.2	0.4	0.6	0.8	1.0
Hardness (HRC)	25.0	25.1	27.5	30.0	32.8	30.6	26.2	24.0	20.2	19.0	18.9

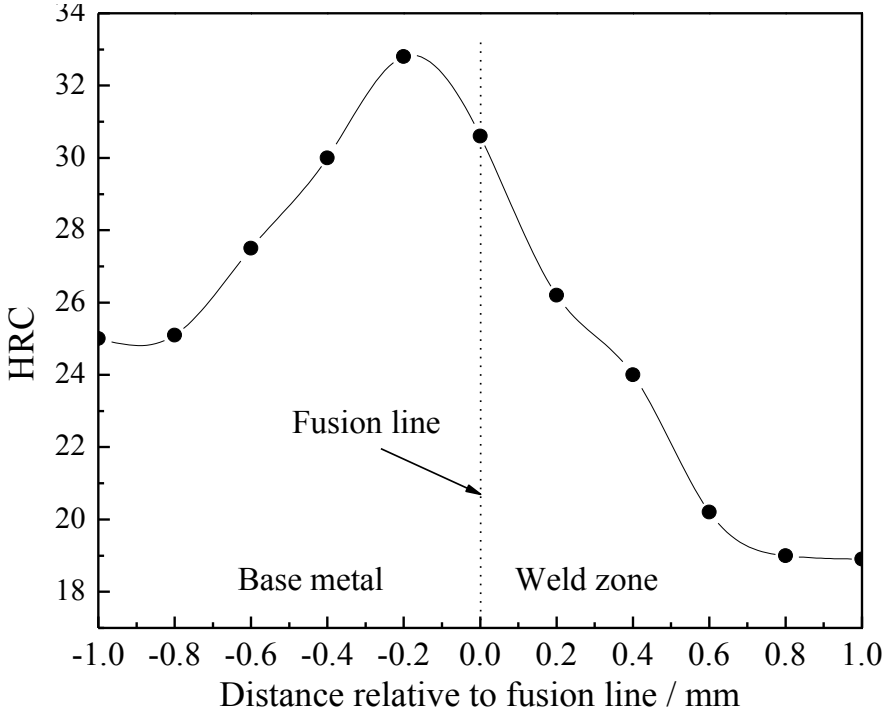

Figure 6. Hardness with dependence on the distances relative to the fusion lines

In summary, the selection of Ni625 welding wire used for the overlay welding treatment on glass-lined tube with a small diameter revealed good qualities in the anticorrosion, mechanical and metallurgical properties. The accelerated corrosion tests in the CO_2 environment successfully simulated the corrosive situation of raw gas and the lower corrosion rate assessed by weight loss method revealed the better corrosion resistance by nickel overlay at the joint part. Furthermore, the potentiodynamic polarization surveys revealed high susceptibility to the pitting initiation of the nickel

materials giving rise to higher current densities relative to the situation of steel. In contrast, the noble nickel can provide long-standing corrosion protection against the general failure of overlay welding treatment. In addition, the comparative studies using the mechanical tensile, bending, hardness and microstructure analyses revealed the better mechanical properties of the joint part after the nickel overlay treatment. With this respect, the proposed Ni625 welding treatment on the carbon steel prior to the butt welding displayed satisfactory qualities for the empirical engineering.

4. CONCLUSIONS

1. The Ni625 undercoat prior the welding process revealed better mechanical qualities relative to that of 20# carbon steels.

2. The weld overlay revealed the absence of general corrosion after CO2 corrosion tests and the weight loss method revealed the corrosion rate at ~4.3±0.1x105 mdd.

3. The higher corrosion current densities of the nickel materials relative to that of the steel in the chloride solutions are due to the high susceptibility of the nickel materials to the pitting initiation.

4. Increasing the temperature of the corrosive environment led to the poorer corrosion protection properties due to the enhanced corrosion events at the metal surface.

ACKNOWLEDGEMENTS
This work has been supported by the National Nature Science Foundation of China (No. 51404286) and the Natural Science Foundation of Shandong Province (No. ZR2014EEQ018).

References

1. Y. Zhou, F. Yan. *Int. J. Electrochem. Sci.,* 11 (2016) 3976.
2. C. Sun, F. Xie, W. Tian, X. Wu. *Oil field equipment*, 05 (2009) 55.
3. K. Videm, A. M. Koren. *Corrosion*, 49 (1993) 749.
4. R. Plaut, C. Herrera, D. Escriba, P. Rios, A. Padiha. *Materials Research*, 10 (2007) 453.
5. B. Li, J. Wang, X. Wang, X. Yue. *Int. J. Electrochem. Sci.,* 11 (2016) 1.
6. X. Mao, X. Liu, R. W. Revie. *Corrosion Science*, 50 (1994) 651.
7. L. Caceres, T. Vargas, L. Herrera. *Corrosion Science*, 51 (2009) 971.
8. Z. Xia, K. C. Chou, Z. Szklarska-Smialowska. *Corrosion*, 45 (1989) 636.
9. C. A. Palacios, J. R. Shadley. *Corrosion*, 47 (1991) 122.
10. E. Zhao. *Standard and quality of petroleum and chemical industry in China*, 08 (2003) 288
11. H. Jin, J. Feng, J. Wang, Y. Wang, X. Chen, X. Zhao. *2006 Forum of corrosion and protection of oil field in west China*, Urumqi, 2006.
12. Z. Zhao, Z. Zhao, X. Mao, Z. Wang. *Welded pipe and tube*, 05 (2015) 22.
13. Y. Han, Y. Wu, G. Li, F. Pan, R. Fan, X. Liu. *Materials Science Forum*, 850 (2016) 1004.
14. Su. X, Lai C, Peng L, et al. *Int. J. Electrochem. Sci*. 11 (2016) 4828.
15. G. Li, D. Sun, Y. He. *Oil and Gas Storage and Transportation*, 17 (1998) 34.
16. L. Liu, J. Han. *Corrosion and Protection*, 32 (2011) 417.
17. X. Wang, J. Pan, H, Zhou, Y. Zhang, Z. Liu. *Hot Working Technology*, 21 (2011) 154.
18. M. Pourbaix. *Altas of Electrochemical Equilibria in Aqueous Solutions*, 2nd English ed., (1974)
19. J. Yang. *Lanzhou: Lanzhou university of technology*, (2011) 21.
20. Z. S. Smialowska. Corrosion Science, 11 (1971) 209.

21. H.-H. Strehblow. *Materials and Corrosion*. 27 (1976) 792.
22. H. Kim, J. W. Johnson. *The Angle Orthodontist*, 69 (1999) 39.
23. J. Liao. *Physics examination and testing*, 03 (2003) 35.